Synthesis and control of generalized dynamically substructured systems

D P Stoten*, **J Y Tu,** and **G Li**
Advanced Control and Test Laboratory (ACTLab) and the Department of Mechanical Engineering, University of Bristol, Bristol, UK

The manuscript was received on 30 May 2008 and was accepted after revision for publication on 27 November 2008.

DOI: 10.1243/09596518JSCE635

Abstract: The experimental technique for testing engineering systems via the method of dynamic substructuring is receiving significant global interest, for example in the fields of large-scale structural, aerospace, and automotive system testing. Dynamically substructured systems (DSSs) enable full-size, critical components of a complete system to be physically tested in real-time, within a laboratory environment, while the remainder of the system is modelled numerically. The intention is that the combined physical–numerical DSS behaves as if it were the complete (or emulated) system.

In an ideal mechanical DSS, for example, perfect synchronization of displacements and forces at the interfaces between the numerical and physical components (or substructures) is required. Hence, a key design feature of successful DSS systems is the high fidelity of the control action. Equally, a DSS controller must be able to cope with non-linear, time-varying, and uncertain parameters within the physical substructure dynamics.

The main purpose of this paper is to present a generalized DSS framework, together with associated linear and adaptive control strategies, that are specifically tailored to achieve high synchronization performance. The initial studies of this problem, as described in an earlier paper by Stoten and Hyde, are therefore continued by generalizing both the DSS dynamics and the control strategies to include (a) a number of newly defined modes of operation and (b) multivariable dynamics. In addition, comparative implementation and simulation studies are included, based upon the DSS testing of a mechanical system (a planar quasi-motorcycle rig), which was specifically designed to highlight the main features of this research. The comparative studies show that excellent DSS control can be achieved, especially with the addition of an adaptive component to the controller, despite significant changes to the physical substructure dynamics.

Keywords: adaptive control, minimal control synthesis algorithm, dynamic substructuring

1 INTRODUCTION

Much attention is currently being given to the technique of dynamically substructured systems (DSSs) by the worldwide dynamic testing community. DSS is a numerical–physical testing strategy, which decomposes a complete, or emulated, system (Σ_E) into two or more substructures. These substructures may be physical (Σ_P) or numerical (Σ_N). Critical, often non-linear, components are tested physically, at full scale, to allow vital dynamical behaviour to be investigated. The remaining parts, which are often dynamically well understood, are modelled in real-time, for example via numerical integration methods or the finite element method. During a test, the decomposed DSS system must be controlled in real-time, so that errors between the synchronization variables at the interfaces are ideally reduced to zero. The DSS system will then replicate the behaviour of Σ_E.

The DSS technique offers certain advantages over more conventional testing schemes [**1**–**4**].

**Corresponding author: Advanced Control and Test Laboratory (ACTLab) and the Department of Mechanical Engineering, University of Bristol, Queen's Building, University Walk, Bristol BS8 1TR, UK. email: d.p.stoten@bristol.ac.uk*

1. Only critical components are tested, avoiding the necessity to test a complete system (which may be impossible in some cases, due to size constraints, impracticality, or lack of existence).
2. Difficulties associated with scale model testing, such as similitude and non-linearity problems, are avoided.
3. Convergence and stability problems associated with purely numerical simulations of the critical components are avoided.
4. Problems associated with non-real-time testing, such as generating accurate derivative-dependent inertial and viscoelastic forces, are avoided.

However, the DSS method also has a number of potential disadvantages, including the necessity for high-quality synchronization control, the lack of a generalized framework for analysis and synthesis, the requirement for real-time numerical simulation, additional sensor requirements at the interfaces with the physical substructures, and the necessity to negate the dynamical effects introduced by the actuation systems within Σ_P.

Much of the work in reference [**1**] focused on solving the synchronization control problem for a generalized single-input/single-output (SISO) structured DSS and a generalized closed-loop scheme was developed, as shown in Fig. 1. In this paper, a substructured system will again be represented by the three terms in Fig. 1, $\{\mathbf{G}_0, \mathbf{G}_1, \mathbf{G}_2\}$, which can be either SISO or multi-input/multi-output (MIMO) substructures, modelled in the transfer function matrix (TFM) or state-space form. For the present, a mainly TFM approach to DSS controller analysis and synthesis is adopted.

In reference [**1**] the three terms, $\{\mathbf{G}_0, \mathbf{G}_1, \mathbf{G}_2\}$, were used to represent a generalized system, yielding the generalized substructures Σ_1 and Σ_2, together with the generalized outputs $\{z_1, z_2\}$, as shown in Fig. 1. For many practical cases $\Sigma_1 = \Sigma_N$ and $\Sigma_2 = \Sigma_P$. Hence, in order to represent the DSS dynamics in a transparent manner and without loss of generality, it will be assumed that $\Sigma_1 = \Sigma_N$ and $\Sigma_2 = \Sigma_P$ in what follows. Thus, the following associations can be made: G_0 is related to Σ_N, G_1 to both Σ_P and Σ_N, and G_2 to the so-called transfer system component of Σ_P. The transfer system consists of the test specimen actuators, sensors, and mechanical support structure. Typically, the transfer system actuators will have their own inner-loop controllers, often proprietary proportional-integral-derivative (PID) systems, which are therefore part of Σ_P and not part of the DSS controller. The latter is shown as the linear substructuring controller (LSC) in Fig. 1 and is comprised of two terms, $\{\mathbf{K}_d, \mathbf{K}_e\}$.

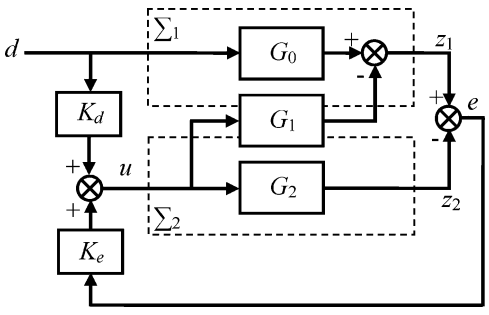

Fig. 1 The generalized substructuring framework of Stoten and Hyde [**1**]

In the figure, $\{d, u\}$ are external excitations and the DSS control signals, while $\{z_1, z_2\}$ are the outputs of the numerical and physical substructures respectively. The two outputs must be in near-perfect synchronization; that is, the substructuring error $(e = z_1 - z_2)$ must always be driven towards zero if a DSS is to function satisfactorily. Synchronization is complicated by the addition of the transfer system, which of course would not be part of the original emulated system, Σ_E. In particular, the transfer system actuators and inner-loop controllers introduce additional gain and phase, which must be compensated for by the DSS controller.

An outer-loop LSC and an adaptive minimal control synthesis with error feedback (MCSEF) algorithm have both been proposed as viable DSS controllers in references [**1**] and [**4**]. Figure 1 shows that LSC is a two-degree-of-freedom (DOF) controller, where (in the SISO case) $\mathbf{K}_e$ is a constant feedback gain and $\mathbf{K}_d$ is a forward loop shaping filter. In the ideal case, $\{\mathbf{K}_d, \mathbf{K}_e\}$ are synthesized from a complete knowledge of the DSS dynamics. However, the effectiveness of the LSC policy will deteriorate in the presence of non-linearities and/or unknowns in the system. Therefore, the adaptive MCSEF algorithm has also been specifically tailored for the control of DSS. The MCSEF controller, which is normally used in parallel with LSC, is of the same structure as the LSC component within Fig. 1. However, in MCSEF, $\mathbf{K}_d$ and $\mathbf{K}_e$ are synthesized as time-varying adaptive gains. The DSS synchronization error dynamics are then ensured to possess the property of global asymptotic stability.

Hence, the principle objective of this paper is to generalize the substructuring framework beyond that presented in reference [**1**] and to develop the associated control synthesis procedure. This involves a discussion of multivariable design, force/displacement substructuring, and various modes of DSS

operation. The rest of this paper is structured as follows. A generalized substructuring framework is presented in section 2, using a purposely constructed quasi-motorcycle (QM) DSS rig to illustrate the concepts. Section 3 provides the basis for the synthesis of MIMO LSC and MCSEF controllers, directly following on from the developments in section 2. In order to introduce the DSS concepts in a relatively straightforward manner, section 4 then details the design, implementation, and comparative test results of a SISO example. Section 5 moves on to describe the synthesis and control of a more complex MIMO DSS, this time using comparative tests via simulation of the dynamic responses. Finally, section 6 draws together the main conclusions from this work.

2 DEVELOPMENT OF A GENERALIZED FRAMEWORK FOR DSS TESTING

This section aims to discuss the generalization of a substructuring framework to MIMO systems. To illustrate the DSS concepts in a transparent manner, a QM DSS is described as the subject for substructuring synthesis and control. The rig, shown in Fig. 2, has been developed as part of the EPSRC (Engineering and Physical Sciences Research Council)-sponsored *ACGDSS* (adaptive control of generalized dynamically substructured systems) project within the University of Bristol's ACTLab (Advanced Control and Test Laboratory) and consists of two horizontally mounted wheel/tyre one-DOF substructures, $\{\Sigma_1, \Sigma_2\}$, and a vertically mounted two-DOF rigid body substructure, Σ_3. Each substructure is mechanically separate from the others and each can be tested in physical or numerical form.

2.1 Generalized framework for a DSS quasi-motorcycle system

A schematic representation of the planar emulated QM system is shown in Fig. 3, together with its equivalent three-substructure decomposition. The emulated system, Σ_E, is comprised of two wheels and tyres with associated mass–spring–damping constants $\{m_1, k_1, c_1\}$ and $\{m_2, k_2, c_2\}$, plus two suspension struts with spring–damper constants $\{k_{31}, c_{31}\}$ and $\{k_{32}, c_{32}\}$, and a rigid vehicle body with inertial properties $\{m_3, J_3\}$. As shown in section 2.2, some or all of the substructured components $\{\Sigma_1, \Sigma_2, \Sigma_3\}$ may be implemented as physical substructures, with the remainder being implemented as numerical substructures. Furthermore, two external road disturbances, $\{d_1, d_2\}$, are assumed to excite $\{\Sigma_1, \Sigma_2\}$, where Σ_1 is considered to be at the front of the vehicle and Σ_2 at the rear.

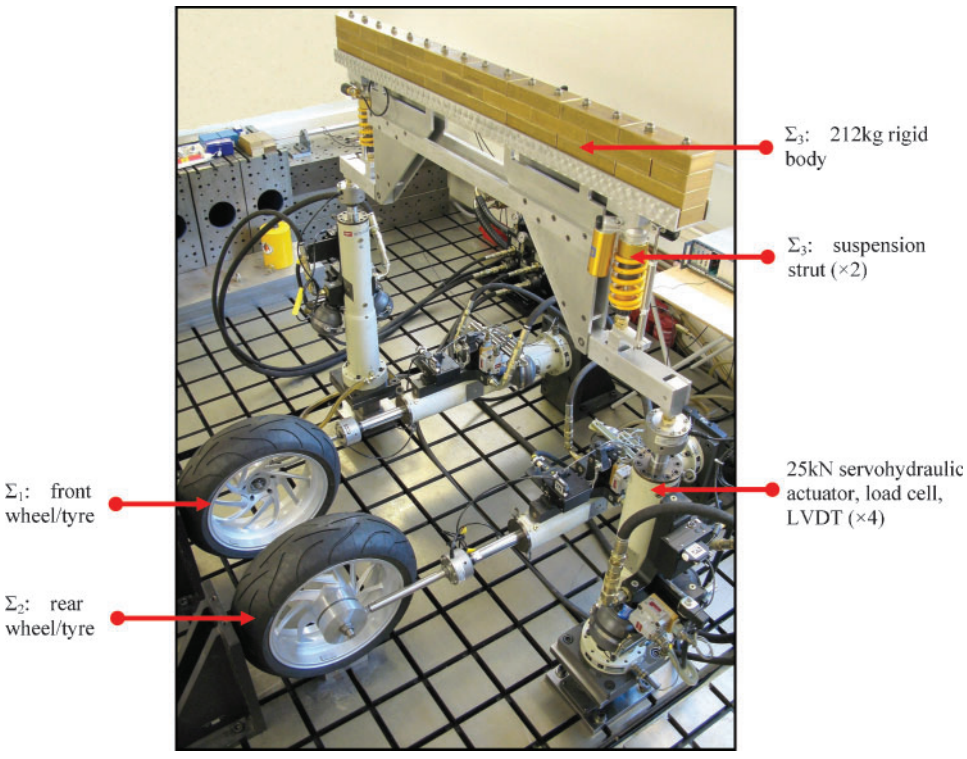

Fig. 2 The quasi-motorcycle DSS test rig showing the three substructures and their actuators

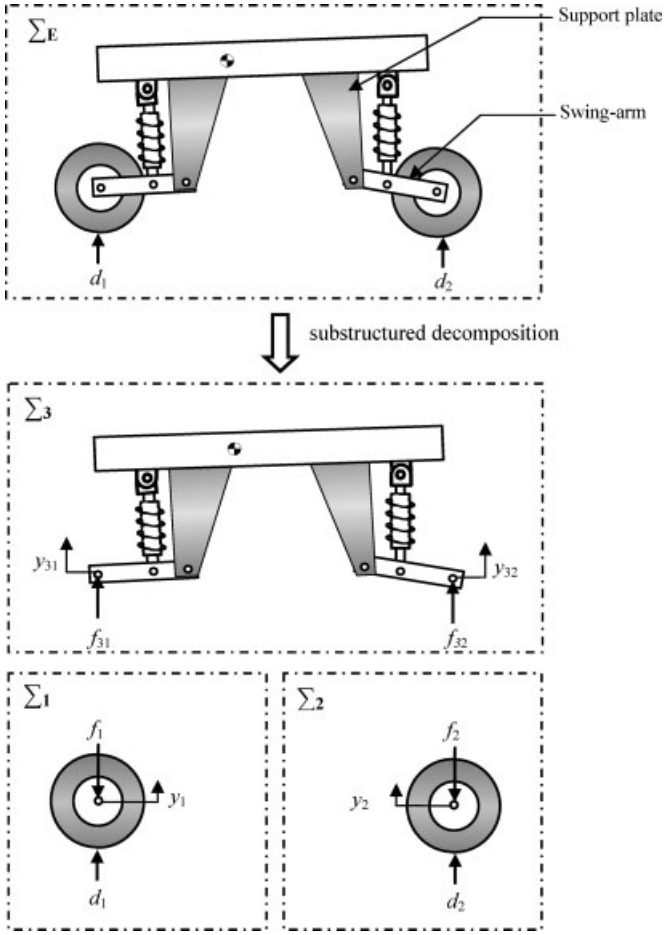

Fig. 3 Schematic representation of the QM rig in its substructured form

The induced displacements and forces at the common attachment point of the front swing-arm and wheel hub are denoted as $\{y_{31}, f_{31}\}$ and $\{y_1, f_1\}$ respectively and $\{y_{32}, f_{32}\}$ and $\{y_2, f_2\}$ for the rear attachment point. Thus, the synchronized variables and dynamic constraints have to be selected from the pairs $\{y_{31}, y_1\}$, $\{y_{32}, y_2\}$, $\{f_{31}, f_1\}$ and $\{f_{32}, f_2\}$. In many DSSs there is a degree of arbitrariness over the selection of these synchronized variables and the interaction constraints. This will be a topic for future research.

In summary, it is noted that the QM system allows for a general investigation of DSS, according to the type of body forces (inertial or reaction) that are imposed, the number and type of substructures (physical or numerical), the dynamic complexity (SISO or MIMO), and the type of synchronization variables (displacement or force).

In the next section the modes of operation (MO) of a DSS system are characterized by reference to the types of body force imposed on the physical substructure, Σ_P. MO characterization is of particular relevance to users of test facilities, where the type of body forces has a profound effect on the hardware that must be used and, as it transpires, the formulation of a DSS controller. For example, in the field of large-scale structural testing, a shaking table would typically be used to impart purely inertial forces, while a reaction frame/wall would be used to impart reaction forces. Furthermore, solutions to combinations of inertial and reaction force DSS testing problems are becoming increasingly necessary.

2.2 QM experimental rig design features

In this section, the original substructuring framework of Fig. 1 is imposed on the QM system, using the concept of the MO of the physical substructure, Σ_P, together with the adoption of the following notation. In Fig. 4(a), for example, $\{\Sigma_1, \Sigma_2\}$ are both physical substructures of the reaction force type and are therefore relabelled as $\{\Sigma_{P1}, \Sigma_{P2}\}$. Similarly, in Fig. 4(b), Σ_3 is a physical substructure of the inertial type and is relabelled Σ_{P3}. However, if either of these two sets are numerical substructures, they are

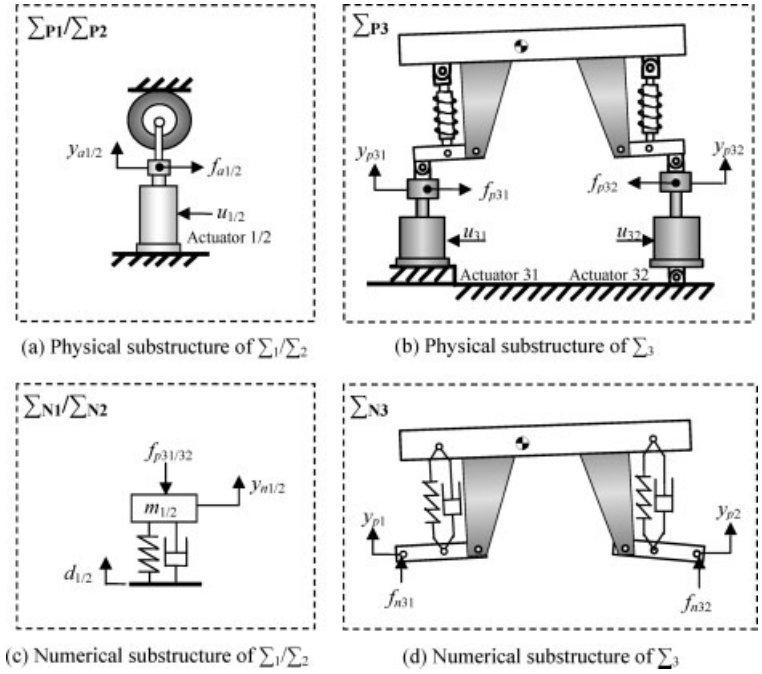

Fig. 4 The illustration of substructured MOs and components for the QM

relabelled $\{\Sigma_{N1}, \Sigma_{N2}\}$ and Σ_{N3} (see Figs 4(c) and (d) respectively). In the actual rig, all physical substructures, Σ_{Pi}, include ± 25 kN servo hydraulic actuators, supported by hydrostatic bearings, to provide the fundamental motion. Note in Fig. 4(b) that the right-hand (rear) actuator 32 of Σ_{P3} is free to rotate in the vertical plane passing through its basal joint, in order to ensure unconstrained kinematic motion of the rig.

Hence, when the DSS contains only one Σ_{Pi}, with one type of force excitation, it is said that it has a single-mode (SiM) of operation. Two or more Σ_{Pi} with the same type of force excitation constitute a multi-mode (MuM) of operation. If the DSS has several Σ_{Pi}, but with different types of force excitation, it is called a mixed-mode (MiM) operation. To complete the set in a logical way, a DSS that is comprised entirely of Σ_{Pi}, of any type, is said to have a physical mode (PhM) of operation and one that has entirely Σ_{Ni} is said to have a numerical mode (NuM) of operation. The NuM is the only member of this set that does not need to be executed in real-time. Although the PhM and the NuM can be considered to be extensions to the normal concept of a DSS, each of them is of significant practical interest in their own right. Thus, controllers that are being developed for the PhM will, for example, enable geographically remote physical experiments to be synchronized to form a seamless whole. Similarly, controllers that are being developed for the NuM are leading to methods of stable synchronization for decentralized numerical problems.

Table 1 summarizes the application of five substructuring MO to the QM system. These MO are typical within mechanical and structural testing environments and are not intended to be an exhaustive taxonomy. The table also indicates that the SiM can be subdivided into SiM1 and SiM2, since the single Σ_P can be in Σ_3 (as Σ_{P3}) or in either of Σ_1 (as Σ_{P1}) or Σ_2 (as Σ_{P2}).

3 DEVELOPMENT OF GENERALIZED DSS CONTROL SYSTEMS

A discussion follows of the basic problem of DSS controller synthesis for the generalized framework with the five MO and then the results are applied to the QM in section 4.

Table 1 Five MO for the QM DSS (P = physical; N = numerical)

	MO 1a SiM1	MO 1b SiM2	MO 2 MuM	MO 3 MiM	MO 4 NuM	MO 5 PhM
Σ_1	N	P(N)	P	P(N)	N	P
Σ_2	N	N(P)	P	N(P)	N	P
Σ_3	P	N	N	P	N	P

3.1 Linear substructuring controller (LSC)

Following the discussion in section 1, LSC is the first DSS controller candidate to be investigated. LSC is based upon a linear model of the underlying dynamics and, from Fig. 1, its control signal is given by

$$u(s) = \mathbf{K}_{\mathrm{d}}(s)d(s) + \mathbf{K}_{\mathrm{e}}(s)e(s) \tag{1}$$

so that the substructuring error signal can be written as

$$\begin{aligned} e(s) &= \mathbf{G}_0(s)d(s) - [\mathbf{G}_1(s) + \mathbf{G}_2(s)]u(s) \\ &= \mathbf{G}_{\mathrm{d}}(s)d(s) - \mathbf{G}_{\mathrm{u}}(s)u(s) \end{aligned} \tag{2}$$

where $\mathbf{G}_{\mathrm{d}} = \mathbf{G}_0$ and $\mathbf{G}_{\mathrm{u}} = \mathbf{G}_1 + \mathbf{G}_2$. Substituting equation (1) into (2), the substructuring error can be re-written as

$$e(s) = [\mathbf{I} + \mathbf{G}_{\mathrm{u}}(s)\mathbf{K}_{\mathrm{e}}(s)]^{-1}[\mathbf{G}_{\mathrm{d}}(s) - \mathbf{G}_{\mathrm{u}}(s)\mathbf{K}_{\mathrm{d}}(s)]d(s) \tag{3}$$

It can be seen that equation (3) implies a two-DOF control solution. The first part of the solution, which assumes perfect knowledge of the DSS dynamics, ensures that $e \to 0$ when

$$\mathbf{K}_{\mathrm{d}}(s) = \mathbf{G}_{\mathrm{u}}^{-1}(s)\mathbf{G}_{\mathrm{d}}(s) \tag{4}$$

given that $\mathbf{G}_{\mathrm{u}}$ is a non-minimum phase and non-singular. Inevitably, parameter variations in Σ_{P} will result in a degraded response from the open-loop solution of equation (4), so that closed-loop stability and robustness must be guaranteed via appropriate synthesis of $\mathbf{K}_{\mathrm{e}}$ to yield desirable roots of the MIMO closed-loop characteristic equation

$$\mathbf{I} + \mathbf{G}_{\mathrm{u}}(s)\mathbf{K}_{\mathrm{e}}(s) = 0 \tag{5}$$

There are many methods to solve for $\mathbf{K}_{\mathrm{e}}$ in equation (5); a simple method is introduced in sections 4.2 and 5.2 that results in a decoupled closed-loop response for all DOFs within Σ_{P}. The diagonal entries of $\mathbf{K}_{\mathrm{e}}$ can then be determined via classical SISO techniques, such as the root loci method.

3.2 Adaptive substructuring controller using an additional minimal control synthesis with error feedback

The minimal control synthesis with error feedback (MCSEF) algorithm is a derivative of the original MCS algorithm [**5**]. MCS is an adaptive, model-referenced control strategy, which requires no *a priori* information on the plant dynamic parameters. Direct online computation of the adaptive, time-varying gains enables the controller to accommodate parameter variations and uncertainties. Conceptually, therefore, MCS is ideally suited to the control of DSS problems. Normally, the MCS algorithm includes a parallel reference model, so that the state error between the model and the plant is ensured to be globally asymptotically stable. SISO MCSEF was developed specifically for substructuring control, in order to mirror the structure of the LSC algorithm [**1**] (see also Fig. 5). MCSEF does not include a reference model per se, but the numerical substructure(s) can be considered to be a replacement for it.

Time-varying MCSEF gains, $\{\mathbf{K}_{\mathrm{d}}(t),\ \mathbf{K}_{\mathrm{e}}(t)\}$, were synthesized in reference [**1**] to completely replace the LSC gains and to ensure global asymptotic stability of e, irrespective of the unknown parameters in Σ_{P}. However, in this current work there is a need to retain the beneficial properties of the model-based LSC controller, while having the option of an additional MCSEF controller within the loop, to cater for unknown parameter variations within Σ_{P}. In effect, the LSC gains can be thought of as initial conditions for the adaptive gains. Hence in Fig. 5 the three TFMs, $\{\mathbf{G}_0',\ \mathbf{G}_1',\ \mathbf{G}_3'\}$, are assumed to represent the combined dynamics of the original DSS together with those of the LSC. The subsequent discussion of MIMO LSC + MCSEF stability is based upon the following principles: (a) the LSC component is designed to be a decoupling controller, and (b) SISO MCSEF has already been shown to be stable when applied to the original DSS framework of Fig. 1 [**1**].

Hence, writing the MCSEF control signal as u', the combined LSC + MCSEF control signal is given by

$$u(s) = \mathbf{K}_{\mathrm{d}}(s)d(s) + \mathbf{K}_{\mathrm{e}}(s)e(s) + u'(s) \tag{6}$$

Substituting equation (6) into (2) gives

$$e(s) = \mathbf{G}_{\mathrm{d}}(s)d(s) - \mathbf{G}_{\mathrm{u}}(s)[\mathbf{K}_{\mathrm{d}}(s)d(s) + \mathbf{K}_{\mathrm{e}}(s)e(s) + u'(s)] \tag{7}$$

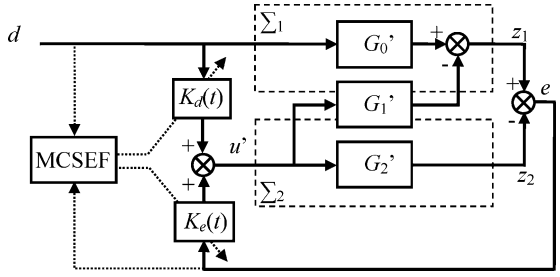

Fig. 5 MCSEF within a substructured environment

which can be rewritten as

$$e(s) = \mathbf{G}'_0(s)d(s) - [\mathbf{G}'_1(s) + \mathbf{G}'_2(s)]u'(s)$$
$$= \mathbf{G}'_d(s)d(s) - \mathbf{G}'_u(s)u'(s) \quad (8)$$

where

$$\mathbf{G}'_{\mathrm{d}}(s) = \mathbf{G}'_0(s) = [\mathbf{I} + \mathbf{G}'_{\mathrm{u}}(s)\mathbf{K}_{\mathrm{e}}(s)]^{-1}[\mathbf{G}_{\mathrm{d}}(s) - \mathbf{G}_{\mathrm{u}}(s)\mathbf{K}_{\mathrm{d}}(s)]$$
$$\mathbf{G}'_{\mathrm{u}}(s) = \mathbf{G}'_1(s) + \mathbf{G}'_2(s) = [\mathbf{I} + \mathbf{G}_{\mathrm{u}}(s)\mathbf{K}_{\mathrm{e}}(s)]^{-1}\mathbf{G}_{\mathrm{u}}(s) \quad (9)$$

Note that equations (2) and (8) have identical structures; therefore the original MCSEF synthesis of reference [**1**] is also valid for the control of DSS when decoupling LSC is already incorporated into the loop.

To complete this section, the form is summarized of the SISO MCSEF algorithm from reference [**1**]. The control signal and adaptive gains are generated according to the following equations

$$u'(t) = \mathbf{K}_{\mathrm{d}}(t)d(t) + \mathbf{K}_{\mathrm{e}}(t)e(t) \quad (10)$$

$$\mathbf{K}_{\mathrm{d}}(t) = \alpha \int_0^t y_{\mathrm{e}}(t)d^{\mathrm{T}}(t)\mathrm{d}t + \beta y_{\mathrm{e}}(t)d^{\mathrm{T}}(t) \quad (11)$$

$$\mathbf{K}_{\mathrm{e}}(t) = \alpha \int_0^t y_{\mathrm{e}}(t)e^{\mathrm{T}}(t)\mathrm{d}t + \beta y_{\mathrm{e}}(t)e^{\mathrm{T}}(t) \quad (12)$$

where $\{\alpha, \beta\}$ are fixed scalar adaptive weights, which are selected empirically; (for example, see reference [**5**] and the comments in section 4.3). The term y_{e} is the output error, generated directly from e, according to

$$y_{\mathrm{e}}(t) = \mathbf{C}_{\mathrm{e}}e(t) \quad (13)$$

where $\mathbf{C}_{\mathrm{e}}$ is selected to ensure a strictly positive real dynamic in the hyperstability proof for the MCSEF controller [**1**, **6**, **7**]. Further comments on these issues are given in the relevant sections 4.3 and 5.3.

4 COMPARATIVE IMPLEMENTATION STUDIES ON A HALF-BODY QUASI-MOTORCYCLE SIM DSS

To illustrate the concept of substructuring framework and controller design, in this section the DSS control of a simplified half-body version of the QM system is presented by way of implementation tests. This is the first experimental verification of the methods developed in reference [**1**]. A more structurally complex MIMO investigation of the QM MiM DSS then follows in section 5.

4.1 Half-body SIM DSS dynamics

Figure 6 shows the half-body emulated system, Σ_{E}, and the corresponding substructured decomposition, $\{\Sigma_{\mathrm{P1}}, \Sigma_{\mathrm{N2}}\}$. In comparison with Figs 3 and 4, the half-body system of Fig. 6 is seen to be equivalent to the front half of the original QM system. In this single-mode substructuring framework, the wheel/tyre is arbitrarily taken to be the physical substructure, Σ_{P1}, and a single suspension strut/translational half-mass as the numerical substructure, Σ_{N2}. The parameters for the half-mass and strut are derived from the original QM system and are shown in Table 2. In the absence of the 3:1 leverage swingarm, the spring and damper constants have been reduced to one-ninth of their original (averaged) values, in order to preserve dynamic similarity.

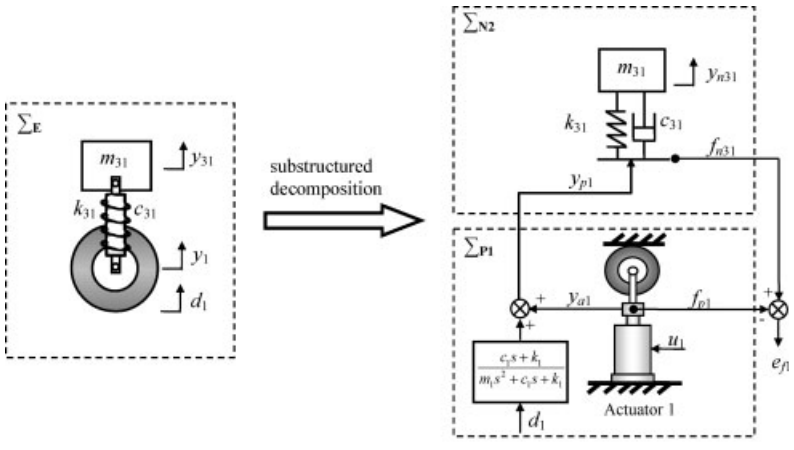

(a) the emulated system (b) the substructured system

Fig. 6 The half-body QM DSS

Table 2 Notation and parameters for the half-body QM DSS

Parameter	Description	Values
m_{31}	Rigid-body mass	102 kg
k_{31}	Suspension spring stiffness	32.3 kN/m
c_{31}	Suspension damping constant	665 N s/m
m_1	Wheel/tyre mass	12.3 kg
k_1	Tyre radial stiffness	384 kN/m
c_1	Tyre radial damping constant	700 N s/m
a_1	Actuator/P-controller denominator coefficient	8.00 s^{-1}
b_1	Actuator/P-controller numerator coefficient	8.00 s^{-1}

In the physical substructure, Σ_{P1}, the contact point on the tyre surface would ideally reproduce the road disturbance, d_1. The displacement response of the wheel hub, in terms of d_1 and the measured hub force f_{p1}, would then be described by

$$y_{p1}(s) = \left(\frac{c_1 s + k_1}{m_1 s^2 + c_1 s + k_1}\right) d_1(s) - \left(\frac{1}{m_1 s^2 + c_1 s + k_1}\right) f_{p1}(s) \tag{14}$$

where $\{m_1, k_1, c_1\}$ are the parameters associated with the linearized dynamics of the wheel and tyre. This configuration would require two actuators. However, in tests a simplified configuration is used for Σ_{P1}, requiring just one actuator and a rigid, non-moving support for the tyre, as shown in Fig. 6. (Note that this simplification could not be used if the dynamics associated with d_1 are unknown.) The wheel hub displacement is measured as y_{a1}

$$y_{a1}(s) = -\left(\frac{1}{m_1 s^2 + c_1 s + k_1}\right) f_{p1}(s) \tag{15}$$

so that from equation (14), the effect of the road displacement is replicated as

$$y_{p1}(s) = \left(\frac{c_1 s + k_1}{m_1 s^2 + c_1 s + k_1}\right) d_1(s) + y_{a1}(s) \tag{16}$$

The reconstructed $y_{p1}(s)$ is then fed back to Σ_{N2} as the interaction constraint. The dynamics of Σ_{P1} are completed via the linear description of the transfer system, which was obtained via a conventional system identification technique

$$f_{p1}(s) = \underbrace{\left(\frac{b_1}{s + a_1}\right)}_{G_{a1}} u_1(s) \tag{17}$$

where $a_1 \approx b_1 \approx 8\,s^{-1}$ in the nominal case. In tests, the inner-loop P-controller gain is used to provide a quantifiable parameter variation within the DSS dynamics; for example, halving the nominal gain leads to $a_1 \approx b_1 \approx 4\,s^{-1}$. However, only nominal parameters are used in the synthesis procedures for all LSC controllers.

Correspondingly, the dynamics of the numerical substructure, Σ_{N2}, are described by

$$y_{n31}(s) = \left(\frac{c_{31} s + k_{31}}{m_{31} s^2 + c_{31} s + k_{31}}\right) y_{p1}(s) \tag{18}$$

$$\begin{aligned} f_{n31}(s) &= (c_{31} s + k_{31})\left[y_{p1}(s) - y_{s31}(s)\right] \\ &= \frac{m_{31} s^2 (c_{31} s + k_{31})(c_1 s + k_1)}{(m_{31} s^2 + c_{31} s + k_{31})(m_1 s^2 + c_1 s + k_1)} d_1(s) \\ &\quad - \frac{m_{31} s^2 (c_{31} s + k_{31}) G_{a1}}{(m_{31} s^2 + c_{31} s + k_{31})(m_1 s^2 + c_1 s + k_1)} u_1(s) \end{aligned} \tag{19}$$

Hence, in terms of the original DSS shown in Fig. 1, the forces f_{n31} and f_{p1} are chosen as the substructure outputs z_1 and z_2 respectively. This implies that the controlled DSS synchronization error is e_{f1}, where

$$\begin{aligned} e_{f1}(s) = z_1(s) - z_2(s) = f_{n31}(s) - f_{p1}(s) &= \underbrace{\frac{m_{31} s^2 (c_{31} s + k_{31})(c_1 s + k_1)}{(m_{31} s^2 + c_{31} s + k_{31})(m_1 s^2 + c_1 s + k_1)}}_{G_d(s)} d_1(s) \\ &\quad - \underbrace{\left(\frac{m_{31} s^2 (c_{31} s + k_{31})}{(m_{31} s^2 + c_{31} s + k_{31})(m_1 s^2 + c_1 s + k_1)} + 1\right) G_{a1}(s)}_{G_u(s)} u_1(s) \end{aligned} \tag{20}$$

4.2 LSC synthesis

Using equation (4) the SISO LSC feedforward gain, $\mathbf{K}_d$, is determined from the corresponding expressions for $\mathbf{G}_u$ and $\mathbf{G}_d$ in equation (20)

$$\mathbf{K}_d(s) = \mathbf{G}_u^{-1}(s)\mathbf{G}_d(s) = \frac{m_{31}s^2(c_{31}s+k_{31})(c_1s+k_1)(s+a_1)}{b_1[m_{31}s^2(c_{31}s+k_{31})+(m_{31}s^2+c_{31}s+k_{31})(m_1s^2+c_1s+k_1)]} \tag{21}$$

Figure 7(a) shows the Bode plot for this expression, clearly indicating its phase advance characteristics. In practice, the non-proper form of equation (21) is implemented in discrete-time via the inclusion of an approximate differentiation term, with due regard to noise suppression at high frequencies. The feedback component, $\mathbf{K}_e$, is a constant gain to be determined, for example, by the root loci method applied to the characteristic equation (5). The resulting loci are shown in Fig. 7(b), where $\mathbf{K}_e = 15$ at the selected root locations, yielding a relatively fast dominant pair of underdamped roots, with a settling time of approximately 0.11 s.

4.3 MCSEF synthesis

Synthesis of the adaptive component of the DSS controller is a relatively simple matter of choosing the scalar weights $\{\alpha, \beta\}$ in equations (11) and (12), and determining the output error matrix, $\mathbf{C}_e$, in equation (13). The initial conditions for the adaptive gains in equations (11) and (12) are arbitrary; when used in conjunction with LSC, a typical choice is $\mathbf{K}_d(0) = 0$ and $\mathbf{K}_e(0) = 0$, reflecting the lack of any prior knowledge of these values.

The choice of the adaptive weights has been discussed in many previous papers on this subject. Essentially, the choice is based on physical or simulation experiments, with the ratio of the weights fixed so that $\alpha = 10\beta$, while α is initially chosen to be a relatively low value, for example $\alpha = 0.01$. This initial choice presupposes that all input/output signals to the adaptive component are scaled to be within a ± 10 V range. Then, if the resulting adaptive convergence is slow, α is increased by a factor of 10; however, if the convergence is fast but noisy, α is decreased by a factor of 10. This process is repeated until a satisfactory convergence is achieved. In the tests described in this section, suitable values of the weights were rapidly determined as $\alpha = 1$ and $\beta = 0.1$.

As was indicated in reference [**1**], a reference model and its associated parameter matrix, $\mathbf{A}_m$, are not necessary in the explicit synthesis of the DSS MCSEF component. However, the concept of an implicit reference model for the stability proof and the synthesis of the error feedback matrix, $\mathbf{C}_e$, is necessary. The solution for $\mathbf{C}_e$ is given by the positive definite solution to the well-known Lyapunov equation

$$\mathbf{A}_m^T\mathbf{P} + \mathbf{P}\mathbf{A}_m = -\mathbf{Q}, \quad \mathbf{C}_e = \mathbf{B}_e^T\mathbf{P} \tag{22}$$

where $\mathbf{Q}$ is an arbitrary positive definite matrix and $\mathbf{B}_e$ is a known input matrix reflecting the structure of the DSS dynamics, for example $\mathbf{B}_e = [0\ 1]^T$ [**1**]. A pragmatic

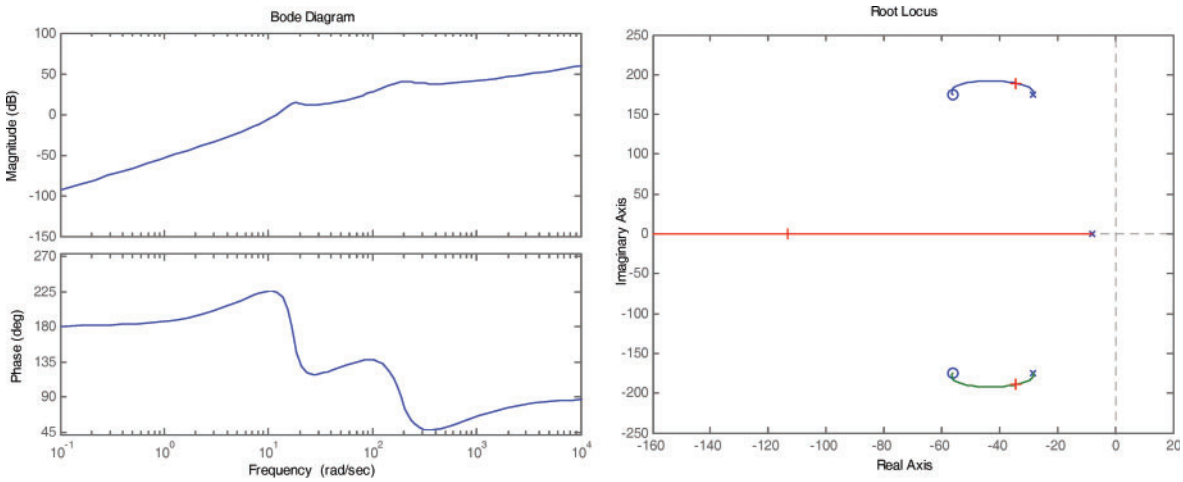

(a) Bode plot of $K_d(s)$ (b) Root loci design for K_e

Fig. 7 The LSC design for the half-body QM DSS

solution to equation (22), described in reference [**1**], is used here, that is $\mathbf{C}_e = 4/t_s$, where t_s is the step-response time of the implicit reference model. In this case, the choice of $t_s = 0.01$ s yields $\mathbf{C}_e = 400$.

4.4 Comparative implementation studies

Tests were conducted on the DSS system in order to compare the performance of LSC and LSC+MCSEF, subject to nominal and changed parameters within the transfer system. Changes were achieved by reducing the inner-loop controller gain by a factor of two, effectively reducing both parameters $\{a_1, b_1\}$ in equation (17) from ~8.0 to ~4.0 s^{-1} and thereby significantly reducing the performance of the actuator system in Σ_P. The road disturbance, d_1, was chosen to be a linear sweep sinusoid, designed to excite the DSS across its sensible frequency spectrum. Parameters associated with this signal were a start frequency of 10 Hz, a final frequency of 0.01 Hz, a span of 20 s, and an amplitude of 2.0 mm. The signal amplitude was initially ramped from 0 to 2 mm over a period of 3.0 s, thus providing a smooth transition in the initial stages of the tests. Figures 8 and 9 show the corresponding results.

The principal comparators of response were chosen as the DSS force error, e_{f1}, the control signals, $\{u_1, u_1'\}$, and the adaptive gains, $\{\mathbf{K}_d(t), \mathbf{K}_e(t)\}$. The DSS controllers, LSC and LSC+MCSEF, were both implemented via an outer-loop *dSpace* 1103 system with a control frequency of 10 kHz and a data recording frequency of 1 kHz. All input–output analogue signals to this controller operated over a range of ± 10 V, with calibration constants of 10 mm/V on displacement and 500 N/V on force.

Thus, the left column of Fig. 8 shows the DSS force error and control under the action of LSC, for the nominal case. The maximum amplitude of error was measured as ~0.05 V (25 N), a relatively small value when compared with the static load of 1000 N. LSC had therefore performed very satisfactorily, indicating the high level of accuracy in both the dynamic modelling and LSC synthesis procedures. As a consequence, the required input from the adaptive component of the LSC+MCSEF controller was also relatively small (see the right column of Fig. 8). It can be observed that a minor improvement was achieved, the peak error being reduced to ~0.04 V (20 N), due to the action of the adaptive gains shown in the bottom graph.

Introducing the parameter changes into Σ_{P1} resulted in the responses shown in Fig. 9. Again, the LSC responses are in the left column and the LSC+MCSEF in the right. It is evident from the gain trajectories that the adaptive component was now more active than before, with a corresponding reduction of peak force error from ~0.11 V (55 N) to ~0.08 V (40 N).

A better indication of controller performance is given in Fig. 10, which shows the integral square error (ISE) curves for each of the four tests described above. Clearly, there was little difference between the controllers in the nominal case. However, when the Σ_P parameters were changed, an increase in the LSC ISE (as measured at the end of the tests) of ~5.5 resulted. With the addition of the adaptive component, this reduced to a factor of ~1.8 – a significant improvement.

It can be noted that the above implementation tests were repeated in a purely simulation environment, with very similar results being obtained. These simulation results are not included here, for the sake of brevity. However, they constituted a major part of a model verification programme that permitted the use of simulated testing of a more complex DSS on the QM rig. One such development, on the MiM DSS, is described in the next section.

5 COMPARATIVE SIMULATION STUDIES ON THE QUASI-MOTORCYCLE MIM DSS

Following the successful SISO implementation tests conducted on the half-body SiM DSS, this section illustrates the application of the MIMO substructuring framework and LSC+MCSEF controller design to a more complex MiM DSS. This is the first verification of the control methodology to be provided, when applied to an MIMO DSS consisting of a mixed MO. Comparative simulation results are presented, illustrating the successful and essential nature of the adaptive component of the controller.

5.1 MiM DSS dynamics

The selection of the QM MiM DSS for the investigations in this section provides a general extension of the previous results from reference [**1**] and from section 4 of this paper. In this new configuration, there is a reaction-force physical substructure Σ_{P1} (the front wheel/tyre), an inertial-force physical substructure Σ_{P3} (the rigid-body/suspension strut system), and a single numerical substructure Σ_{N2} (the rear wheel/tyre). Furthermore, the overall problem has a MIMO structure with mixed substructuring error signals; that is, one force and two

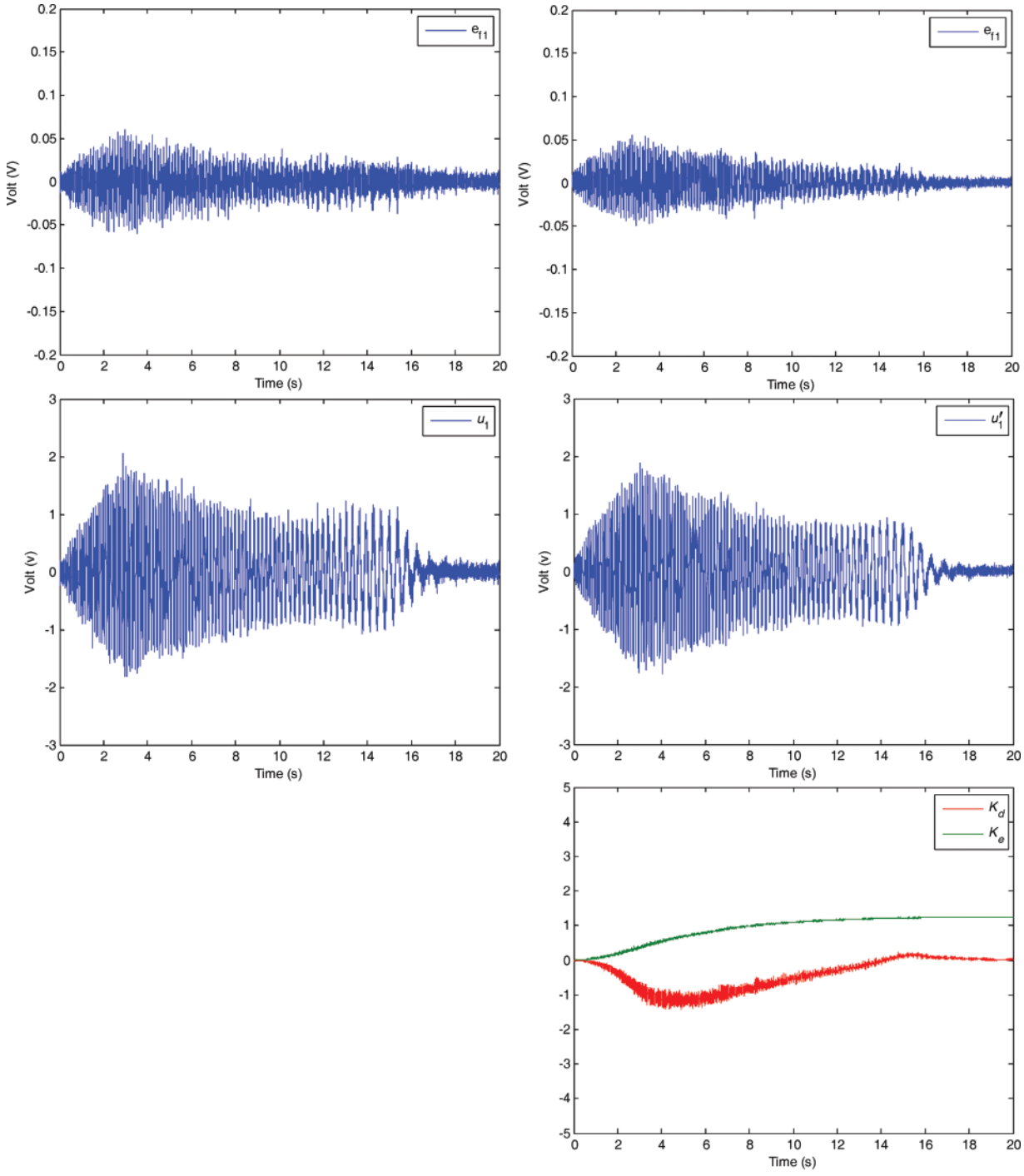

(a) LSC responses
top: DSS error, e_{f1}
bottom: control, u_1

(b) LSC+MCSEF responses
top: DSS error, e_{f1}
middle: control, u_1'
bottom: MCSEF gains, $\{K_d, K_e\}$

Fig. 8 LSC and LSC + MCSEF responses with nominal parameter values

displacement pairs of outputs must be synchronized in order to achieve satisfactory DSS performance.

As shown in Fig. 11, a single actuator is again used within Σ_{P1} to generate the front wheel hub motion, y_{p1}, via dynamic compensation of the road disturbance term, d_1. In the rigid-body/suspension strut substructure, Σ_{P3}, there are two actuators, resulting in displacement signals $\{y_{p31}, y_{p32}\}$ and force signals

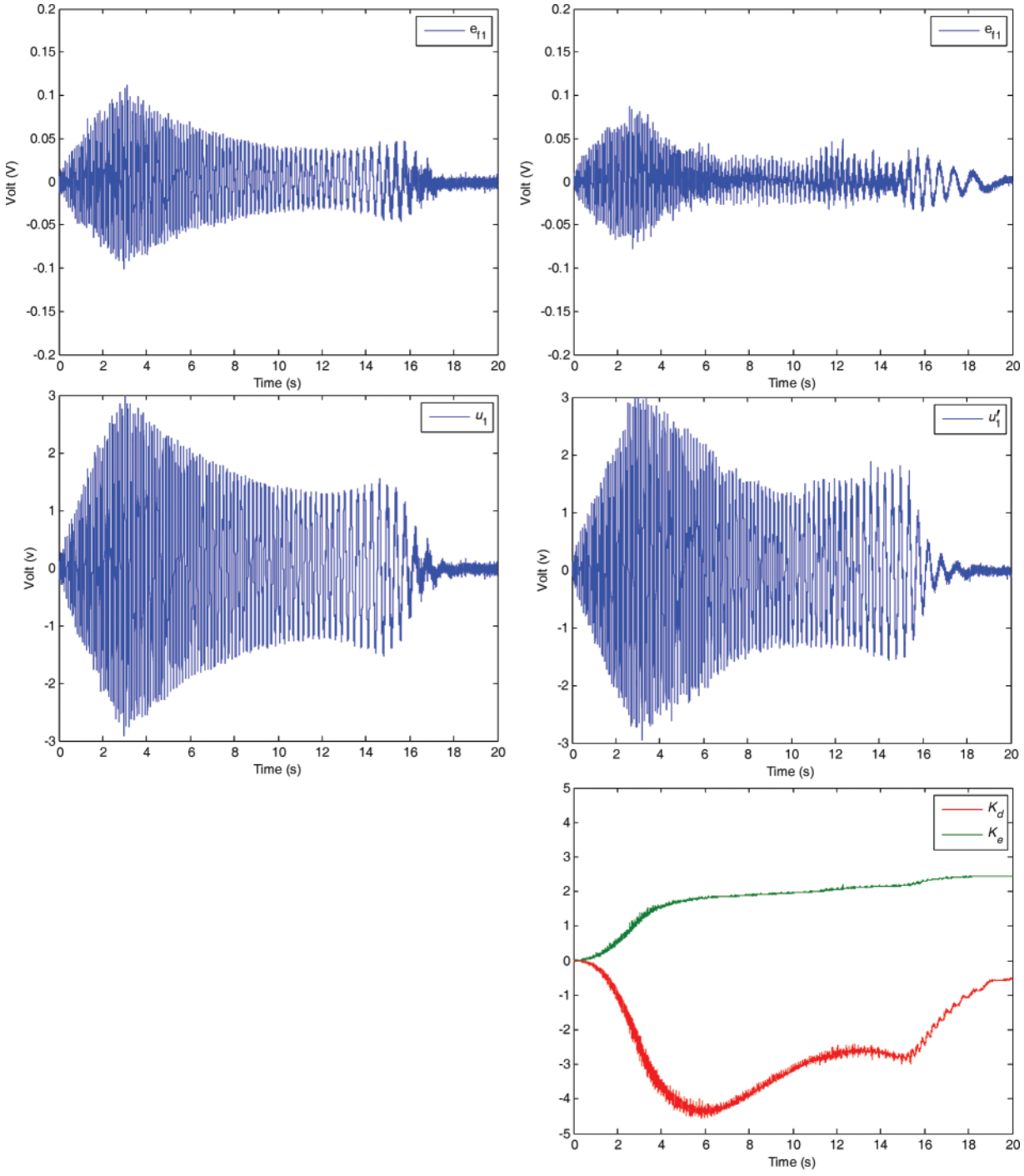

(a) LSC responses
top: DSS error, e_{fl}
bottom: control, u_1

(b) LSC+MCSEF responses
top: DSS error, e_{fl}
middle: control, u_1'
bottom: MCSEF gains, $\{K_d, K_e\}$

Fig. 9 LSC and LSC + MCSEF responses with changed parameter values

(f_{p31}, f_{p32}). The interaction constraint in the system is between the rear wheel/tyre numerical substructures Σ_{N2} and Σ_{P3}, with f_{p32} being fed back from Σ_{P3} to Σ_{N2}. Hence, the synchronization pairs are $\{y_{p31}, y_{p1}\}$, $\{y_{p32}, y_{n2}\}$, and $\{f_{p31}, f_{p1}\}$, so that the DSS control problem is to reduce the associated errors, $e_{y1} = y_{p1} - y_{p31}$, $e_{y2} = y_{n2} - y_{p32}$, and $e_{f1} = f_{p31} - f_{p1}$, towards zero.

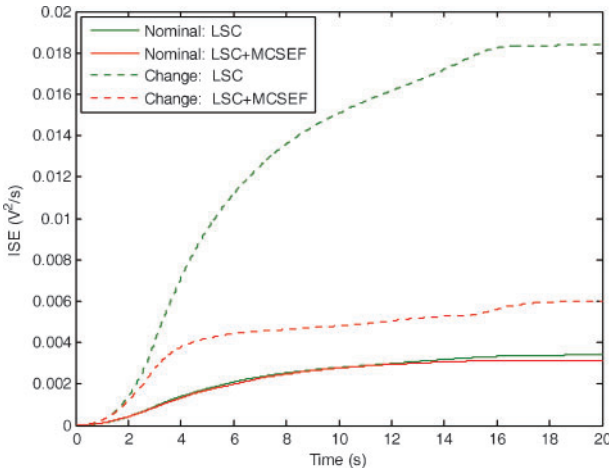

Fig. 10 ISE curves for the DSS errors shown in Figs 8 and 9

In the rest of this section linear relationships are generated, which are then used in the synthesis of the LSC controller in section 5.2. However, full non-linear expressions are used in the corresponding simulations of the DSS control in section 5.4. Expressions for the DSS dynamics can be obtained in a similar manner to those for the half-body system. First of all, the equations of motion are obtained for the front wheel/tyre physical substructure, Σ_{P1}

$$y_{\mathrm{p1}}(s)=\underbrace{\left(\frac{c_1 s+k_1}{m_1 s^2+c_1 s+k_1}\right)}_{G_{11}(s)} d_1(s)-\underbrace{\left(\frac{1}{m_1 s^2+c_1 s+k_1}\right)}_{G_{12}(s)} f_{\mathrm{p1}}(s) \tag{23}$$

where the actuator force, f_{p1}, is determined via the model identified for the inner-loop P-controller/actuator 1

$$f_{\mathrm{p1}}(s)=\underbrace{\left(\frac{b_1}{s+a_1}\right)}_{G_{\mathrm{a1}}} u_1(s) \tag{24}$$

Similarly, the equation of motion for the rear wheel/tyre numerical substructure, Σ_{N2}, is

$$y_{\mathrm{n2}}(s)=\underbrace{\left(\frac{c_2 s+k_2}{m_2 s^2+c_2 s+k_2}\right)}_{G_{21}(s)} d_2(s) - \underbrace{\left(\frac{1}{m_2 s^2+c_2 s+k_2}\right)}_{G_{22}(s)} f_{\mathrm{p32}}(s) \tag{25}$$

Turning to the rigid-body component of the physical substructure, Σ_{P3}, the fact is used that the 3:1 leverage in the swing-arms reduces the suspension struts' spring and damper constants by a factor of 9. Assuming that all other dynamic effects due to the swing-arm rotations are negligible, a linearized model of Σ_{P3} is then equivalent to the model synthesized in reference [**4**], where no swing-arms were present and where the suspension struts were connected directly to the actuators. The simplified rigid-body system shown in Fig. 12 is then used to generate the equations of motion for Σ_{P3}. Note that

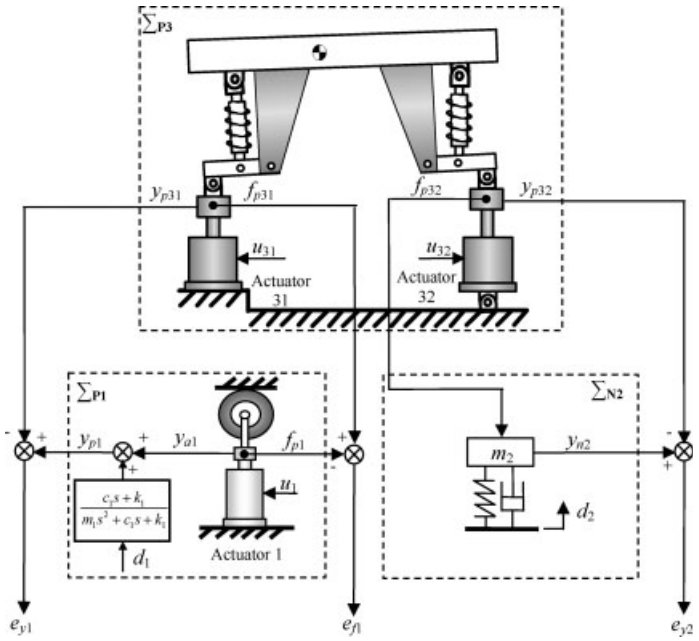

Fig. 11 The mixed-mode substructured system

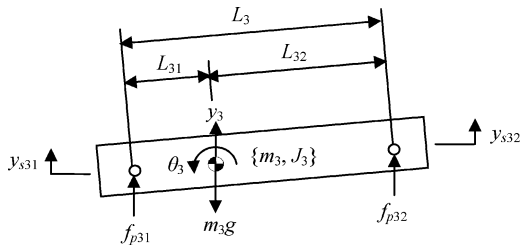

Fig. 12 The simplified free-body diagram of the QM rigid-body system

the coordinate pair $\{y_{s31}, y_{s32}\}$ refers to the vertical displacements of the body, measured along the projected longitudinal axes of actuators 31 and 32.

Hence for small angles of rotation, the linearized equations in heave and pitch of the rigid body, about its centre of mass, are given by

$$m_3\ddot{y}_3 = f_{p31} + f_{p32} - m_3g \tag{26}$$

$$J_3\ddot{\theta}_3 = L_{32}f_{p32} - L_{31}f_{p31} \tag{27}$$

and the corresponding linearized equations for the kinematics are

$$\theta_3 = \frac{y_{s32} - y_{s31}}{L_3} \tag{28}$$

$$y_3 = \frac{L_{32}}{L_3}y_{s31} + \frac{L_{31}}{L_3}y_{s32} \tag{29}$$

Using linear suspension strut models, $\{y_{s31}, y_{s32}\}$ can be written in terms of $\{y_{p31}, y_{p32}\}$ as

$$y_{s3j}(s) = \left(\frac{c_{3j}s + k_{3j}}{m_{3j}s^2 + c_{3j}s + k_{3j}}\right)y_{p3j}(s), \quad j = 1, 2 \tag{30}$$

In a manner similar to the above, the dynamics of the inner-loop controllers/actuators 31 and 32 can be written as

$$y_{p3j}(s) = \underbrace{\left(\frac{b_{3j}}{s + a_{3j}}\right)}_{G_{a3j}}u_{3j}(s), \quad j = 1, 2 \tag{31}$$

where $G_{a3j}(s)$ $(j = 1, 2)$ are the corresponding transfer system dynamics. Rearranging equation (26) to (31) results in the following expressions for the forces $\{f_{p31}, f_{p32}\}$

$$\begin{aligned} f_{p31}(s) &= P_2s^2y_{s31}(s) + P_3s^2y_{s32}(s) \\ &= P_2\underbrace{\left[\frac{s^2(c_{31}s + k_{31})}{m_{31}s^2 + c_{31}s + k_{31}}\right]}_{G_{31}(s)}G_{a31}(s)u_{31}(s) \\ &\quad + P_3\underbrace{\left[\frac{s^2(c_{32}s + k_{32})}{m_{32}s^2 + c_{32}s + k_{32}}\right]}_{G_{32}(s)}G_{a32}(s)u_{32}(s) \end{aligned} \tag{32}$$

$$\begin{aligned} f_{p32}(s) &= P_3s^2y_{s31}(s) + P_1s^2y_{s32}(s) \\ &= P_3\underbrace{\left[\frac{s^2(c_{31}s + k_{31})}{m_{31}s^2 + c_{31}s + k_{31}}\right]}_{G_{31}(s)}G_{a31}(s)u_{31}(s) \\ &\quad + P_1\underbrace{\left[\frac{s^2(c_{32}s + k_{32})}{m_{32}s^2 + c_{32}s + k_{32}}\right]}_{G_{32}(s)}G_{a32}(s)u_{32}(s) \end{aligned} \tag{33}$$

where P_1, P_2, and P_3 are equivalent masses given by

$$\begin{aligned} P_1 &= \left(\frac{m_3L_{31}^2}{L_3^2} + \frac{J_3}{L_3^2}\right), \quad P_2 = \left(\frac{m_3L_{32}^2}{L_3^2} + \frac{J_3}{L_3^2}\right) \\ P_3 &= \left(\frac{m_3L_{31}L_{32}}{L_3^2} - \frac{J_3}{L_3^2}\right) \end{aligned} \tag{34}$$

Accordingly, equation (33) can be substituted into equation (25) to obtain y_{n2}, which is required in the formulation of the numerical substructure, Σ_{N2}.

In summary, the expression for the MiM DSS generalized output z_1 (see Fig. 1) can be defined as

$$z_1(s) = \begin{bmatrix} f_{p31}(s) \\ y_{p1}(s) \\ y_{n2}(s) \end{bmatrix} = \mathbf{G}_0(s)\underbrace{\begin{bmatrix} d_1(s) \\ d_2(s) \end{bmatrix}}_{d(s)} - \mathbf{G}_1(s)\underbrace{\begin{bmatrix} u_1(s) \\ u_{31}(s) \\ u_{32}(s) \end{bmatrix}}_{u(s)} \tag{35}$$

where, from the expressions given in equations (23) to (25) and (31) to (33)

$$\mathbf{G}_0 = \begin{bmatrix} 0 & 0 \\ G_{11}(s) & 0 \\ 0 & G_{21}(s) \end{bmatrix} \tag{36}$$

$$\mathbf{G}_1(s) = \begin{bmatrix} 0 & -P_2G_{31}(s)G_{a31}(s) & -P_3G_{32}(s)G_{a32}(s) \\ G_{12}(s)G_{a1}(s) & 0 & 0 \\ 0 & P_3G_{22}(s)G_{31}(s)G_{a31}(s) & P_1G_{22}(s)G_{32}(s)G_{a32}(s) \end{bmatrix} \tag{37}$$

Similarly, the MiM DSS generalized output z_2 can be determined from equations (24) and (31) as

$$z_2(s)=\begin{bmatrix} f_{\mathrm{p}1}(s) \\ y_{\mathrm{p}31}(s) \\ y_{\mathrm{p}32}(s) \end{bmatrix}=\mathbf{G}_2(s)\underbrace{\begin{bmatrix} u_1(s) \\ u_{31}(s) \\ u_{32}(s) \end{bmatrix}}_{u(s)} \tag{38}$$

where

$$\mathbf{G}_2(s)=\begin{bmatrix} G_{\mathrm{a}1}(s) & 0 & 0 \\ 0 & G_{\mathrm{a}31}(s) & 0 \\ 0 & 0 & G_{\mathrm{a}32}(s) \end{bmatrix} \tag{39}$$

In this case, z_1 is composed of both numerical and physical substructure responses, whereas z_2 is composed of entirely physical substructure responses. Now $\{\mathbf{G}_0, \mathbf{G}_1, \mathbf{G}_2\}$ can be used to generate the transfer function matrices $\{\mathbf{G}_{\mathrm{d}}, \mathbf{G}_{\mathrm{u}}\}$ in equation (2), which constitute the basis of the LSC design

$$\mathbf{G}_{\mathrm{d}}(s)=\mathbf{G}_0(s), \quad \mathbf{G}_{\mathrm{u}}(s)=\mathbf{G}_1(s)+\mathbf{G}_2(s) \tag{40}$$

5.2 LSC synthesis

Using equations (35) and (38), the error given by $e=z_1-z_2$ can be written in the form of equation (2), so that the MIMO LSC equation is (see equation (1))

$$\underbrace{\begin{bmatrix} u_1 \\ u_{31} \\ u_{32} \end{bmatrix}}_{u}=\underbrace{\begin{bmatrix} K_{\mathrm{d}11} & K_{\mathrm{d}12} \\ K_{\mathrm{d}21} & K_{\mathrm{d}22} \\ K_{\mathrm{d}31} & K_{\mathrm{d}32} \end{bmatrix}}_{K_{\mathrm{d}}}\underbrace{\begin{bmatrix} d_1 \\ d_2 \end{bmatrix}}_{d}+\underbrace{\begin{bmatrix} K_{\mathrm{e}11} & K_{\mathrm{e}12} & K_{\mathrm{e}13} \\ K_{\mathrm{e}21} & K_{\mathrm{e}22} & K_{\mathrm{e}23} \\ K_{\mathrm{e}31} & K_{\mathrm{e}32} & K_{\mathrm{e}33} \end{bmatrix}}_{K_{\mathrm{e}}}\underbrace{\begin{bmatrix} e_{\mathrm{f}1} \\ e_{\mathrm{y}1} \\ e_{\mathrm{y}2} \end{bmatrix}}_{e} \tag{41}$$

It can be verified from equations (37), (39), and (40) that $\mathbf{G}_{\mathrm{u}}$ is non-minimum phase and non-singular, so that the six entries of the LSC forward gain matrix, $\mathbf{K}_{\mathrm{d}}$, can be determined from equation (4) and the parameter values in Table 3. For example, the resulting Bode plot of $K_{\mathrm{d}11}$ is shown in Fig. 13(a), which is typical of the entire set. Again, the phase advance nature of the forward gain is evident.

As before, closed-loop stability is guaranteed by the LSC error feedback gain matrix, $\mathbf{K}_{\mathrm{e}}$. In this MIMO case, the terms $K_{\mathrm{e}ii}$ $(i=1, 2, 3)$ on the leading diagonal can be simple proportional gains, for example determined by the root loci method. The decoupled closed-loop characteristic equations are then given by

$$1+F_i(s)K_{\mathrm{e}ii}=0, \quad i=1, 2, 3 \tag{42}$$

In equation (42)

Table 3 Notation and parameters for the QM DSS

Parameter	Description	Values
Vehicle rigid body		
m_3	Mass	212 kg
m_{31}, m_{32}	Effective masses at the front and rear ends	102 kg, 110 kg
J_3	Moment of inertia about the centre of mass	75.0 kg m^2
L_3	Length	1.70 m
L_{31}, L_{32}	Lengths from the front and rear ends to the centre of mass	0.882 m, 0.818 m
L_{b}	Swing-arm length	0.300 m
L_{s}	Length between the strut base and actuator attachment	0.200 m
Front and rear suspension struts		
k_{31}, k_{32}	Suspension spring constants	32.3 kN/m, 29.4 kN/m
c_{31}, c_{32}	Suspension damping constants	665 N s/m, 306 N s/m
Front and rear wheels/tyres		
m_1, m_2	Masses	12.3 kg, 15.7 kg
k_1, k_2	Tyre radial stiffnesses	384 kN/m, 405 kN/m
c_1, c_2	Tyre radial damping constants	700 N s/m, 816 N s/m
Inner-loop (P) controllers and actuators		
a_{31}, a_{32}, a_1	Denominator coefficients	25.8 s^{-1}, 25.8 s^{-1}, 8.00 s^{-1}
b_{31}, b_{32}, b_1	Numerator coefficients	25.8 s^{-1}, 25.8 s^{-1}, 8.00 s^{-1}

$$\begin{bmatrix} F_1(s) \\ F_2(s) \\ F_3(s) \end{bmatrix} = \begin{bmatrix} G_{u11} - \left(\dfrac{G_{u12}(G_{u21}G_{u33} - G_{u23}G_{u31}) + G_{u13}(G_{u31}G_{u22} - G_{u32}G_{u21})}{G_{u22}G_{u33} - G_{u23}G_{u32}} \right) \\ G_{u22} - \left(\dfrac{G_{u21}(G_{u12}G_{u33} - G_{u13}G_{u32}) + G_{u23}(G_{u32}G_{u11} - G_{u31}G_{u12})}{G_{u11}G_{u33} - G_{u13}G_{u31}} \right) \\ G_{u33} - \left(\dfrac{G_{u31}(G_{u13}G_{u22} - G_{u12}G_{u23}) + G_{u32}(G_{u23}G_{u11} - G_{u21}G_{u13})}{G_{u11}G_{u22} - G_{u12}G_{u21}} \right) \end{bmatrix} \tag{43}$$

where, to achieve decoupling, the off-diagonal entries of $\mathbf{K}_e$ are assigned in terms of the gains K_{eii} ($i = 1, 2, 3$), as follows

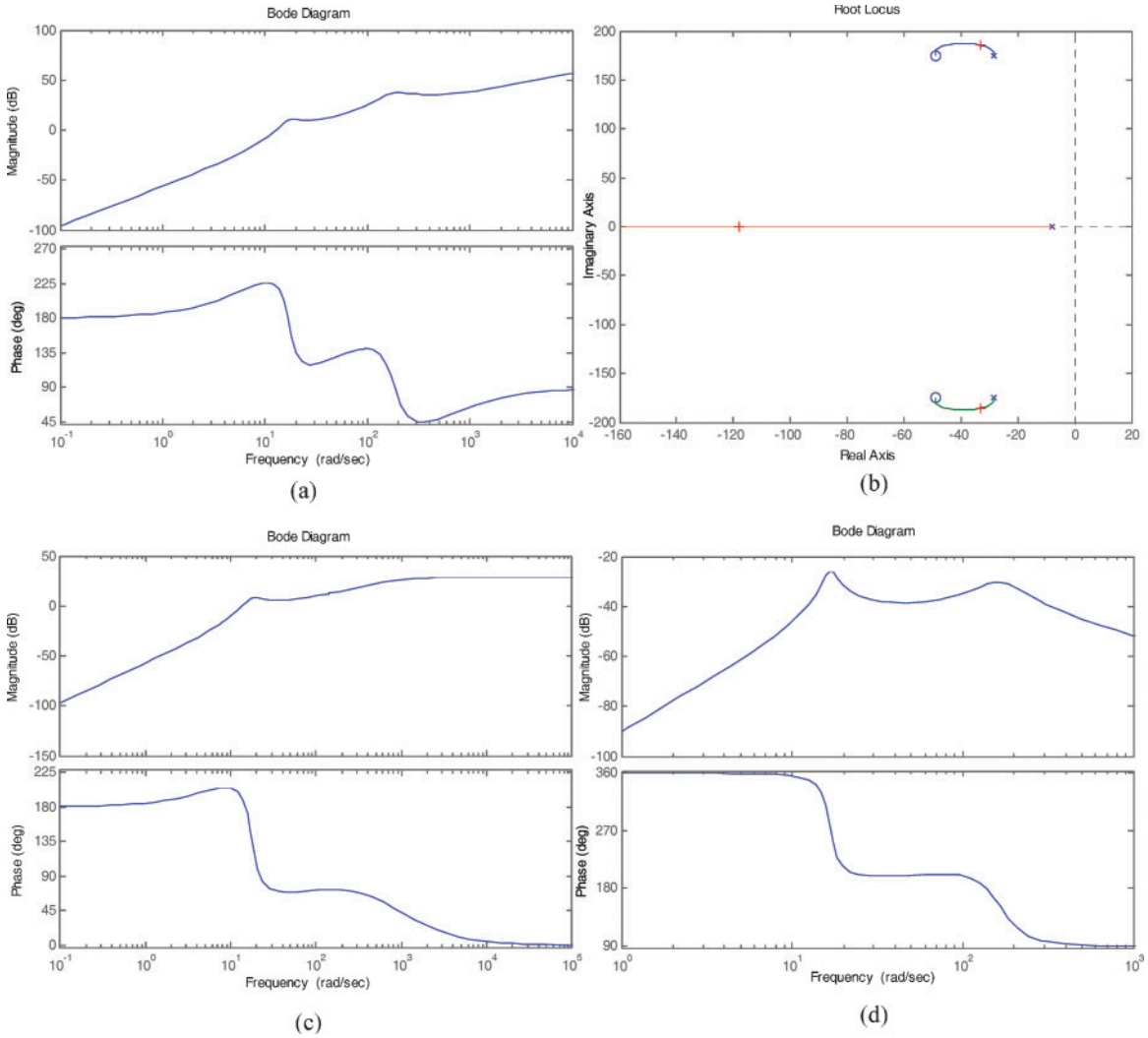

Fig. 13 Examples of the MiM DSS LSC designs: (a) Bode plot for $K_{d11}(s)$; (b) Root loci plot for K_{e11}; (c) Bode plot for $K_{e12}(s)$; (d) Bode plot for $K_{e32}(s)$

$$\begin{bmatrix} K_{e12}(s) \\ K_{e13}(s) \\ K_{e21}(s) \\ K_{e23}(s) \\ K_{e31}(s) \\ K_{e32}(s) \end{bmatrix} = - \begin{bmatrix} 0 & \dfrac{G_{u12}G_{u33} - G_{u13} - G_{u32}}{G_{u11}G_{u33} - G_{u13}G_{u31}} & 0 \\ 0 & 0 & \dfrac{G_{u13}G_{u22} - G_{u12}G_{u23}}{G_{u11}G_{u22} - G_{u12}G_{u21}} \\ \dfrac{G_{u21}G_{u33} - G_{u23}G_{u31}}{G_{u22}G_{u33} - G_{u23}G_{u32}} & 0 & 0 \\ 0 & 0 & \dfrac{G_{u11}G_{u23} - G_{u13}G_{u21}}{G_{u11}G_{u22} - G_{u12}G_{u21}} \\ \dfrac{G_{u22}G_{u31} - G_{u21}G_{u32}}{G_{u22}G_{u33} - G_{u23}G_{u32}} & 0 & 0 \\ 0 & \dfrac{G_{u11}G_{u32} - G_{u12}G_{u31}}{G_{u11}G_{u33} - G_{u13}G_{u31}} & 0 \end{bmatrix} \begin{bmatrix} K_{e11} \\ K_{e22} \\ K_{e33} \end{bmatrix} \tag{44}$$

Examples of some of the corresponding designs from equations (42) to (44) are shown in Figs 13(b) to (d). Thus, in Fig. 13(b), the root loci design for K_{e11} is shown; this design is very similar to the half-body case, with a value of $K_{e11} = 15$ yielding a dominant pair of roots and an associated $t_s \sim 0.12$ s. Arbitrarily, Figs 13(c) and (d) show the Bode plots for K_{e12} and K_{e32} respectively; yet again, the phase advance characteristic in the filter designs is evident.

5.3 MCSEF synthesis

As in section 4.3, synthesis for the adaptive component of the DSS controller involves the selection of the scalar weights $\{\alpha, \beta\}$ in equations (11) and (12), and the determination of the output error matrix, $\mathbf{C}_e$, in equation (13). Simulation studies indicated that the choice of $\alpha = 1$, $\beta = 0.1$ was again suitable for this case. Furthermore, the decoupled nature of the adaptive synthesis allows for the same pragmatic solution for $\mathbf{C}_e$, when $t_s = 0.01$ s

$$\mathbf{C}_e = \left(\frac{4}{t_s}\right) I_3 = 400 I_3 \tag{45}$$

5.4 Comparative simulation studies

In a similar manner to section 4.4, tests were conducted on the MiM DSS system in order to compare the performance of LSC and LSC + MCSEF, subject to nominal and changed parameters within the transfer system. As indicated in sections 5.1 and 5.2, a linear model of the DSS dynamics was used for the LSC synthesis, but a non-linear model of the DSS dynamics was used to generate the simulated results described below.

Changes were implemented by reducing all three inner-loop controller gains by a factor of two. For the MiM DSS, there were two road disturbances, $\{d_1, d_2\}$, which were both chosen to be swept sinusoids with start frequencies of 10 Hz, final frequencies of 0.01 Hz, spans of 20 s, amplitudes of 2.0 mm, and a 0.85 s pure delay between the signals, giving $d_2(t) = d_1(t - 0.85)$. Again, the signal amplitudes were initially ramped from 0 to 2 mm over a period of 3.0 s, providing a smooth transition in the initial stages of test. Figures 14 and 15 show the corresponding results.

As before, in the nominal case, the left-hand column of Fig. 14 shows the DSS errors and controls under the action of LSC. The maximum amplitudes of the errors, $\{e_{f1}, e_{y1}\ e_{y2}\}$, were measured as ~0.04 V (20 N), ~0.025 V (0.25 mm), and ~0.02 V (0.2 mm) respectively. LSC had therefore performed very satisfactorily, the relatively small DSS errors reflecting the mismatch between the LSC design, based upon a linear model of the underlying dynamics and the non-linear model used in the simulation.

The right-hand column of Fig. 14 shows the errors under LSC + MCSEF control. Although the peak errors are of similar magnitudes (equivalent to ~20 N; ~0.15 mm; ~0.1 mm) to those under LSC control, it is clear that the error trajectories themselves are much improved. Hence, the adaptive component of the controller has a significant role, even in this nominal case, since it is required to compensate for the non-linear effects in the system, which LSC alone is unable to do.

Introducing the parameter changes into all three actuator dynamics within Σ_P resulted in the responses shown in Fig. 15, with LSC in the left column and LSC + MCSEF in the right. A noticeable decrease in the resulting DSS error amplitudes occurred with LSC + MCSEF and, as is evident from the control and gain trajectories, a significant increase in adaptive effort was necessary to achieve this.

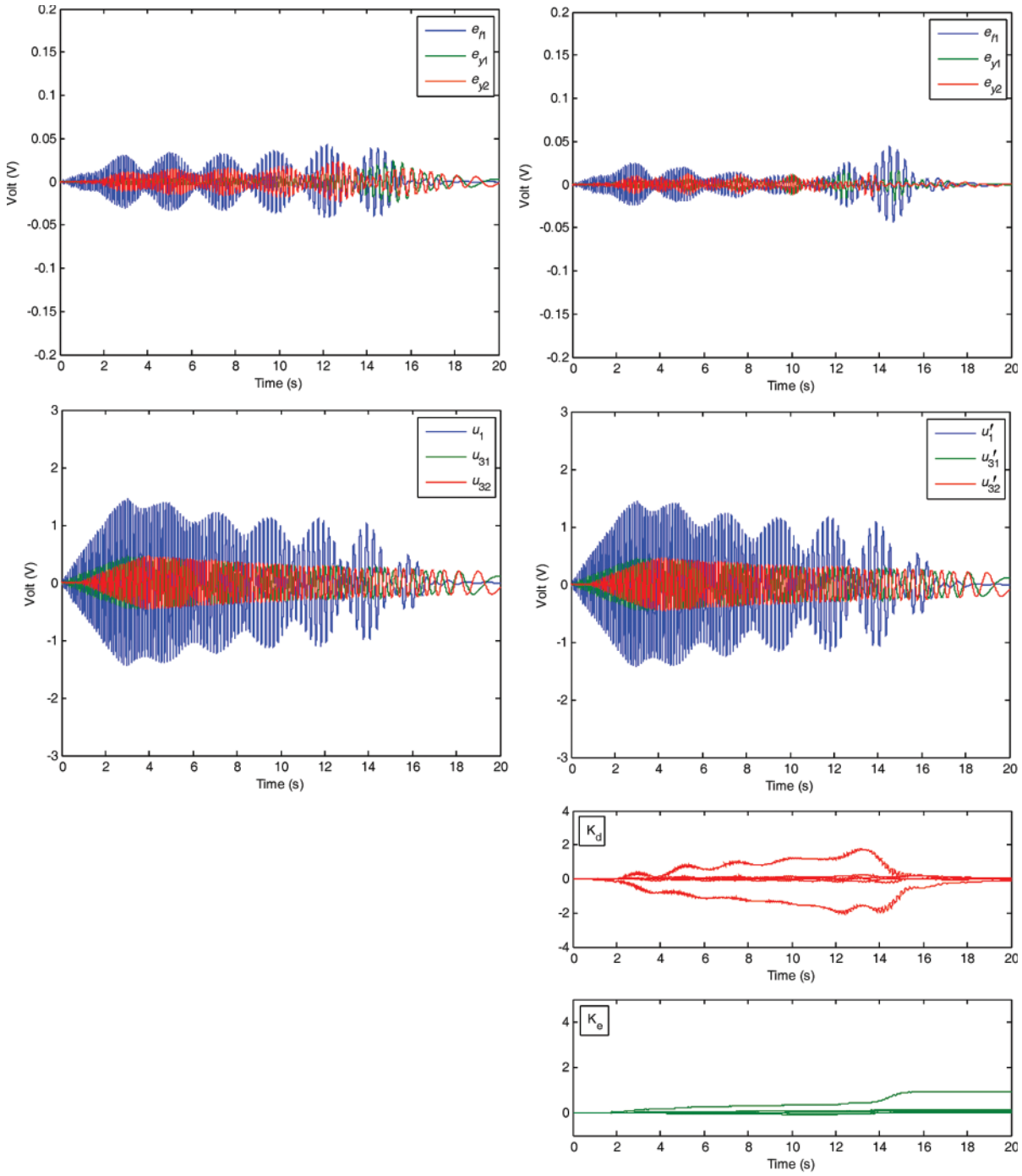

(a) LSC responses
top: DSS errors, e_{f1}, e_{y1}, e_{y2}
bottom: controls, u_1, u_{31}, u_{32}

(b) LSC+MCSEF responses
top: DSS errors, e_{f1}, e_{y1}, e_{y2}
middle: controls, u_1', u_{31}', u_{32}'
bottom: MCSEF gains, $\{K_d, K_e\}$

Fig. 14 LSC and LSC + MCSEF responses with nominal parameter values

The corresponding ISE curves in Fig. 16 again provide a clearer demonstration of performance, with each curve showing the sum of the individual ISEs for the errors, $\{e_{f1}, e_{y1}, e_{y2}\}$. It is evident that LSC + MCSEF has provided an approximately 2.5-fold decrease in ISE when compared with the LSC only case, in both the nominal and changed parameter cases.

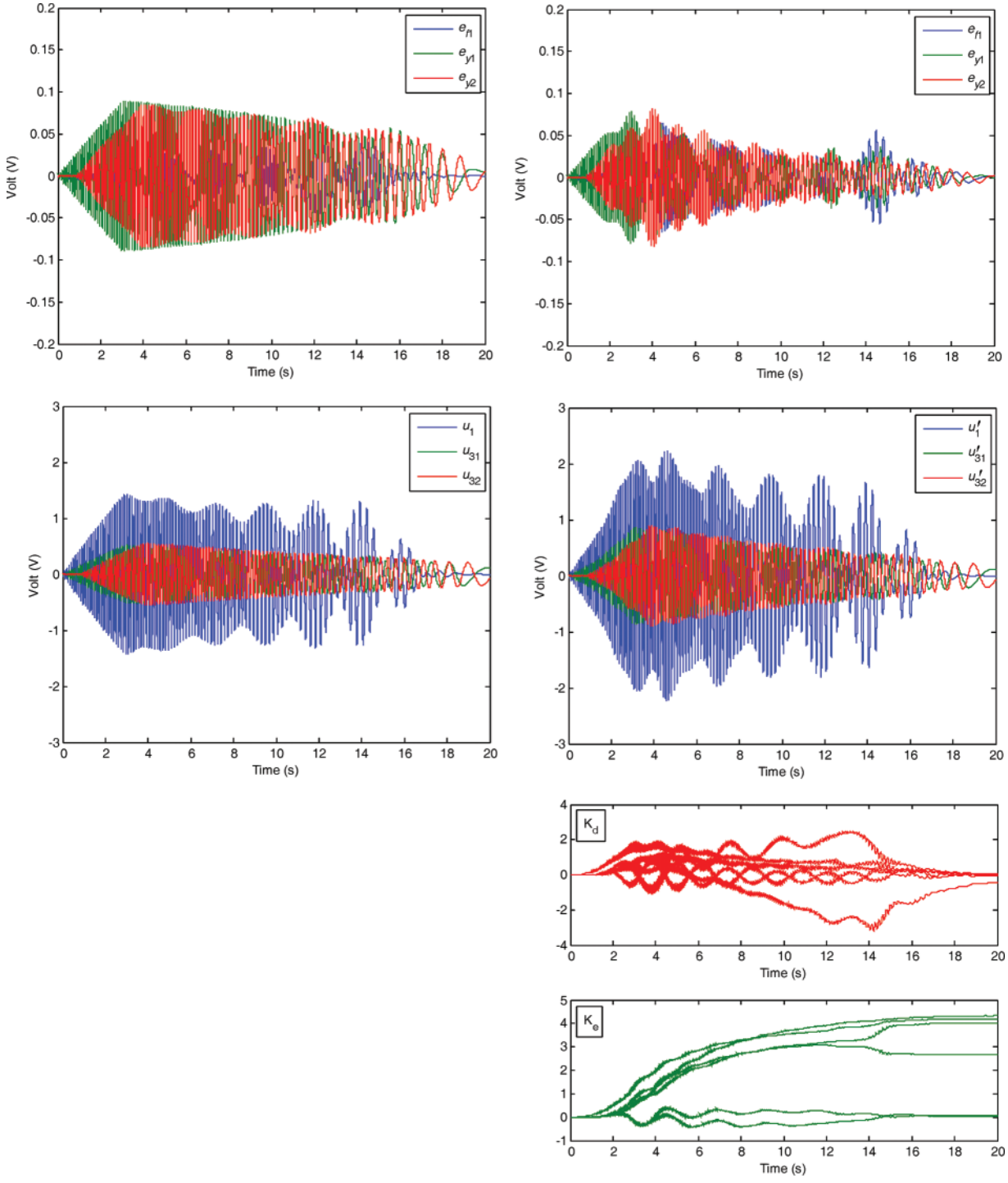

(a) LSC responses
top: DSS errors, e_{f1}, e_{y1}, e_{y2}
bottom: controls, u_1, u_{31}, u_{32}

(b) LSC+MCSEF responses
top: DSS errors, e_{f1}, e_{y1}, e_{y2}
middle: controls, u_1', u_{31}', u_{32}'
bottom: MCSEF gains, $\{K_d, K_e\}$

Fig. 15 LSC and LSC + MCSEF responses with changed parameter values

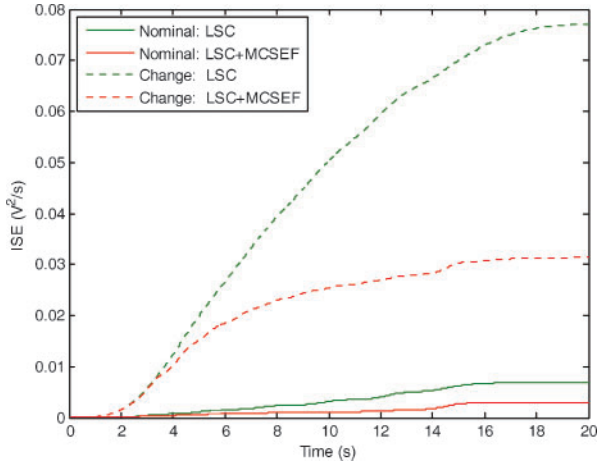

Fig. 16 ISE curves for the DSS errors shown in Figs 14 and 15

6 CONCLUSIONS AND FUTURE WORK

The main conclusions to be drawn from this work are as follows.

1. A generalized framework for dynamically substructured systems (DSS) has been established, based upon the modes of operation of the physical substructures, Σ_P. The new substructuring framework encompasses MIMO dynamics, either in TFM or in state-space form. In this paper, the focus has been on the TFM form.
2. It has been shown that the DSS framework can be used to synthesize a linear substructuring controller (LSC) via classical SISO techniques, thus providing a basis for achieving the exacting levels of substructure synchronization that are required. However, it was also established that LSC performance degrades as parameter uncertainty within Σ_P increases.
3. An extension of the adaptive minimal control synthesis (MCS) algorithm, which incorporates error feedback (EF), has been synthesized for the DSS problem. The new algorithm, MCSEF, can be viewed as an adaptive version of LSC, which mirrors the configuration of the original LSC scheme.
4. LSC and MCSEF are normally used in parallel with one another for DSS control.
5. Experimental implementations and simulations of the proposed methods, on a quasi-motorcycle test rig, showed that the addition of an adaptive MCSEF component enabled excellent synchronization of DSS substructures, despite the presence of significant parameter uncertainties in the actuator dynamics. The combined LSC + MCSEF controller outperformed LSC in every case.

A discussion of the authors' future work in this field now follows. This work will primarily focus on the further development of the generalized dynamic framework of DSS and the corresponding synthesis and analysis of new LSC- and MCSEF-based controllers, using both TFM and state-space descriptions. In particular, further experimental verification of the new DSS concepts will feature significantly in future work. Also to be addressed is the development of the NuM for solving decentralized numerical problems.

The effect of dynamic parameter variations within the experimental programme have so far centred on the Σ_P actuator dynamics, since such variations are relatively simple to implement, they are repeatable, and they represent a commonly encountered problem in DSS testing. Effects of parameter variations elsewhere in the DSS system have been extensively studied via simulations, which are not reported here. As with the experimental investigations, the overall result of changing mass distribution or suspension compliance was found to have a minimal effect on the DSS synchronization error when MCSEF was included within the loop. Part of the future work will include a systematic experimental investigation of such effects on the quasi-motorcycle rig.

In this paper, the size of permissible substructuring error has not been addressed. In practice, the constraint on maximum error will depend on the specific application and the minimum error achievable will depend on the system dynamics (including non-linearities), the actuation bandwidth, sensor noise, and the control algorithm. Ongoing work by the authors using the framework presented here, combined with H_∞ and other optimal robust control methods, will place the permissible substructuring error as a key design parameter, an approach that is expected to provide additional insights.

Finally, the issue of whether to use displacement synchronization (with force as an interaction constraint) or force synchronization (with displacement as an interaction constraint), or a combination of these, has not yet been resolved. Preliminary results show that different modes of operation yield different levels of conditioning of the controllers, depending on the synchronization variables that are used. Thus, another objective of our future research will be to solve this problem and thereby generate best-conditioned DSS control strategies.

ACKNOWLEDGEMENT

The authors gratefully acknowledge the support of the UK Engineering and Physical Science Research Council, Grant EP/D036917, *The adaptive control of generalised dynamically substructured systems*, in the pursuance of this work.

REFERENCES

1 **Stoten, D. P.** and **Hyde, R. A.** Adaptive control of dynamically substructured systems: the single-input, single-output case. *Proc. IMechE, Part I: J. Systems and Control Engineering*, 2006, **220**(I1), 63–79.
2 **Williams, M. S.** and **Blakeborough, A.** Laboratory testing of structures under dynamic loads: an introductory review. *Phil. Trans. R. Soc. Lond. A*, 2001, **359**, 1651–1669.
3 **Blakeborough, A., Williams, M. S., Darby, A. P.,** and **Williams, D. M.** The development of real-time substructure testing. *Phil. Trans. R. Soc. Lond. A*, 2001, **359**, 1869–1891.
4 **Stoten, D. P., Tu, J.-Y.,** and **Li, G.** Adaptive control of generalised dynamically substructured systems. In 17th IFAC World Congress, Seoul, Korea, 2008, pp. 14090–14095.
5 **Stoten, D. P.** A minimal controller synthesis adaptive algorithm for environmental systems. In *Science et Technique du Froid*, 1989, pp. 277–286.
6 **Popov, V. M.** *Hyperstability of automatic control systems*, 1973 (Springer-Verlag, Berlin).
7 **Landau, I. D.** *Adaptive control – the model reference approach*, 1979 (Marcel Dekker, New York).

APPENDIX

Notation

a_i	inner-loop system denominator coefficient
$\mathbf{A}_\mathrm{m}$	reference model parameter matrix
b_i	inner-loop system numerator coefficient
$\mathbf{B}_\mathrm{e}$	structural input matrix
c_i, c_{ij}	viscous damper coefficients
$\mathbf{C}_\mathrm{e}$	output error matrix
d_i	disturbance
e, e_i, e_{ij}	substructuring errors
f_i, f_{ij}	non-specific force outputs
$f_{\mathrm{n}i}$, $f_{\mathrm{n}ij}$	numerical substructure force outputs
$f_{\mathrm{p}i}$, $f_{\mathrm{p}ij}$	physical substructure force outputs
g	acceleration constant due to gravity
$G_{\mathrm{a}i}$, $G_{\mathrm{a}ij}$	transfer system transfer functions
$\mathbf{G}_i$	non-specific substructure transfer function matrix
$\mathbf{I}$	identity matrix
J_i	moment of inertia
k_i, k_{ij}	linear spring coefficients
$\mathbf{K}_\mathrm{d}$	forward gain/transfer function
$\mathbf{K}_\mathrm{e}$	feedback gain/transfer function
L_i, L_{ij}	lengths
m_i, m_{ij}	masses
$\mathbf{P}$	symmetric positive-definite solution to a Lyapunov equation
P_i	equivalent mass
$\mathbf{Q}$	symmetric positive-definite term in a Lyapunov equation
s	Laplace transform variable
t	continuous time
t_s	step-response settling time
u_i, u_{ij}	linear control inputs
u'_i, u'_{ij}	total control inputs (adaptive + linear)
$y_{\mathrm{a}i}$, $y_{\mathrm{a}ij}$	transfer system (actuator) displacement outputs
y_e	output error
y_i, y_{ij}	non-specific displacement outputs
$y_{\mathrm{n}i}$, $y_{\mathrm{n}ij}$	numerical substructure displacement outputs
$y_{\mathrm{p}i}$, $y_{\mathrm{p}ij}$	physical substructure displacement outputs
z_i	generalized substructure output
α	weight on integral adaption
β	weight on proportional adaption
θ_i	angle
Σ_E	emulated system
Σ_i	non-specific substructure
Σ_n, $\Sigma_{\mathrm{n}i}$	numerical substructure
Σ_p, $\Sigma_{\mathrm{p}i}$	physical substructure

Abbreviations

ACGDSS	adaptive control of generalized dynamically substructured systems
ACTLab	(University of Bristol) Advanced Control and Test Laboratory
DOF	degree of freedom
DSS	dynamically substructured system
EF	error feedback
EPSRC	(UK) Engineering and Physical Sciences Research Council
ISE	integral square error
LSC	linear substructuring controller
LVDT	linear variable displacement transformer
MCS	minimal control synthesis

MCSEF	minimal control synthesis with error feedback	PhM	physical mode
MiM	mixed mode	NuM	numerical mode
MIMO	multi-input/multi-output	QM	quasi-motorcycle (experimental rig)
MuM	multi mode	SiM	single mode
MO	mode of operation	SISO	single-input/single-output
		TFM	transfer function matrix